Solving the Structure of Size-Selected Pt Nanocatalysts Synthesized by Inverse Micelle Encapsulation

Beatriz Roldan Cuenya,*,[†,‡,§] Jason R. Croy,[†] Simon Mostafa,[†,§] Farzad Behafarid,[†]
Long Li,[‖] Zhongfan Zhang,[‖] Judith C. Yang,[‖] Qi Wang,[⊥] and Anatoly I. Frenkel*,[⊥]

*Department of Physics, Nanoscience and Technology Center, and Department of Civil, Construction
and Environmental Engineering, University of Central Florida, Orlando, Florida 32816, Department
of Mechanical Engineering and Materials Science, University of Pittsburgh, Pittsburgh,
Pennsylvania 15261, and Department of Physics, Yeshiva University,
New York, New York 10016*

Received March 9, 2010; E-mail: roldan@physics.ucf.edu; anatoly.frenkel@yu.edu

Abstract: The structure, size, and shape of γ-Al$_2$O$_3$-supported Pt nanoparticles (NPs) synthesized by inverse micelle encapsulation have been resolved via a synergistic combination of imaging and spectroscopic tools. It is shown that this synthesis method leads to 3D NP shapes even for subnanometer clusters, in contrast to the raft-like structures obtained for the same systems via traditional deposition-precipitation methods. Furthermore, a high degree of atomic ordering is observed for the micellar NPs in H$_2$ atmosphere at all sizes studied, possibly due to H-induced surface reconstruction in these high surface area clusters. Our findings demonstrate that the influence of NP/support interactions on NP structure can be diminished in favor of NP/adsorbate interactions when NP catalysts are prepared by micelle encapsulation methods.

1. Introduction

Metal nanoparticles (NPs) possess unique properties as compared to their bulk counterparts, including enhanced chemical reactivity. It has recently been recognized that the NP shape might play a crucial role in its catalytic performance. Specifically, it has been demonstrated that different crystallographic facets stabilized on particles with different shapes may result in different reactivities and selectivities.[1−5] For example, the rate of styrene oxidation over Ag nanocube NPs was found to be 14 times higher than over nanoplates, and 4 times higher than over nearly spherical NPs. These differences were attributed to highly reactive {100} facets on the nanocubes, in contrast to the {111} facets present on the nanoplates, and the mixture of {100} and {111} planes in the nanospheres. Similar findings have been made for Pt nanocatalysts that are extensively used in industrial applications.[6] Tian et al.[5] reported the superior catalytic activity of tetrahexahedral Pt NPs with high-index facets [{730},{210},{520}] for the electro-oxidation of formic acid and ethanol as compared to NPs with spherical shapes. This result was attributed to the increased number of atomic

steps and kinks present in their system. Komanicky et al.[4] described the role played by the NP shape on the oxygen reduction reaction over Pt NPs prepared by electron beam lithography. On the basis of the distinct electrocatalytic activities observed for differently oriented NP arrays, the authors suggested the preferential adsorption of O$_2$ on {100} facets and its subsequent diffusion to nearby {111} facets, where it could be more efficiently reduced.

While knowledge of the average cluster size and size distribution characteristics of a particular as-prepared sample is necessary, this is not sufficient for the complete understanding of catalyst reactivity. In fact, information on the most stable cluster shapes under any given set of reaction conditions (temperature, pressure, chemical environment) is equally important. Mittendorfer et al.[7] theoretically predicted drastic changes in the morphology and equilibrium shape of Pd and Rh nanocrystals upon O$_2$ adsorption, with closed-packed {111} facets dominating under low O$_2$ pressures, and nanocrystal rounding occurring at elevated O$_2$ pressures due to its higher adsorption energy on the initially less stable {110} open surfaces. Grazing incidence X-ray diffraction and transmission electron microscopy (TEM) experiments by Nolte et al.[8] on Rh NPs supported on MgO(001) indicated an increase in the total area of {100} facets at the expense of {111} surfaces upon oxidation. Such shape changes were found to be reversible upon subsequent NP reduction during CO oxidation. High-resolution TEM images, obtained by Giorgio et al.[9,10] under H$_2$ and O$_2$ atmospheres using an environmental TEM demonstrated the faceting of TiO$_2$-supported Au NPs under H$_2$ (truncated

† Department of Physics, University of Central Florida.
‡ Nanoscience and Technology Center, University of Central Florida.
§ Department of Civil, Construction and Environmental Engineering, University of Central Florida.
‖ University of Pittsburgh.
⊥ Yeshiva University.
(1) Narayanan, R.; El-Sayed, M. A. *Nano Lett.* **2004**, *4*, 1343.
(2) Narayanan, R.; El-Sayed, M. A. *J. Phys. Chem. B* **2004**, *108*, 5726.
(3) Xu, R.; Wang, D.; Zhang, J.; Li, Y. *Chem. Asian J.* **2006**, *1*, 888.
(4) Komanicky, V.; Iddir, H.; Chang, K. C.; Menzel, A.; Karapetrov, G.; Hennessy, D.; Zapol, P.; You, H. *J. Am. Chem. Soc.* **2009**, *131*, 5732.
(5) Tian, N.; Zhou, Z.-Y.; Sun, S.-G.; Ding, Y.; Wang, Z. L. *Science* **2007**, *316*, 732.
(6) Vaarkamp, M.; Miller, J. T.; Modica, F. S.; Koningsberger, D. C. *J. Catal.* **1996**, *163*, 294.

(7) Mittendorfer, F.; Seriani, N.; Dubay, O.; Kresse, G. *Phys. Rev. B* **2007**, *76*, 233413.
(8) Nolte, P.; Stierle, A.; Jin-Phillip, N. Y.; Kasper, N.; Schulli, T. U.; Dosch, H. *Science* **2008**, *321*, 1654.

octahedron shape), and their rounding and dewetting under O_2. In analogy to the previous observation of Rh clusters, the latter shape changes also appeared to be reversible. These studies demonstrate that chemisorption-induced morphological changes in NPs need to be considered when models to explain catalytic reactivity are proposed, since certain reaction environments might lead to a decrease/increase in the relative area of the most catalytically active surface facets/sites.

Although significant progress in the in situ structural characterization of nanomaterials has been made in the past decade,[7−16] most of the studies have been unable to quantify geometrical properties of real-world nanocatalysts. The major challenge toward the goal of precise three-dimensional characterization is the requirement to discern many competing influences on the NP structure and shape, most notably the effects of the substrate, absorbate, size,[17] and alloying elements and their spatial distribution within the NP.[18] While the studies of size-selected clusters by advanced electron microscopy[19] and diffraction[20] methods offer a high level of detail, and some of these methods are now used in reactive environments and variable temperatures, their spatial resolution is currently limited to about 0.07 Å. X-ray absorption fine-structure (XAFS) spectroscopy is a powerful alternative and/or complement to imaging methods due to its sensitivity to the local atomic environment (the bond lengths can be determined with the accuracy of 0.01 Å or better), adaptability to a wide range of nanocatalysts (ideally in the size range from subnanometer to ∼5 nm), and in situ experimental conditions. However, one limitation of this technique is its ensemble averaging of the local structure over all absorbing atoms in the sample, rendering ill-defined structural results for systems with broad size distributions.[21] Only in the case of well-defined model NPs (in the size range of 2 nm and larger) was it possible to explore the greatest potential of this technique, using it to determine the size, shape, structure, and surface orientation of a very few model systems made just for this purpose.[16,22] Recently, new approaches for the fabrication of nanostructures have enabled us to produce model catalyst samples with narrow NP size and shape distributions.[23−25] These synthesis methods are particularly attractive for systematic investigations of the properties of NPs in the most intriguing nm-size range (<2 nm) that is least investigated experimentally. These methods open up the possibility of characterizing well-defined sizes and shapes of individual NPs by performing ensemble measurements on bulk quantities of nearly identical NPs.

In this article, we demonstrate how extended XAFS (EXAFS) spectroscopy can be used to deduce the cluster shape in Pt/γ-Al_2O_3 nanocatalysts synthesized by inverse micelle encapsulation. In addition, by tuning NP synthesis parameters such as the molecular weight of the encapsulating polymer or the metal/polymer ratio, we were able to synthesize Pt NPs with octahedron, truncated octahedron, and cuboctahedron shapes. Nanoparticle shape determination in these samples is achieved here through an integrated methodology that combines multiple-scattering analysis of EXAFS data with results obtained by other complementary techniques including scanning transmission electron microscopy (STEM), scanning tunneling microscopy (STM), and atomic force microscopy (AFM). In our XAFS experiments, the sensitivity to shape and local structure was greatly enhanced by carrying out the measurements under a hydrogen atmosphere that partially lifts surface disorder. Our measurements demonstrate that our NP preparation method (micellar encapsulation) enables the achievement of predominantly high surface area 3D NPs in the nm-size range of interest to most catalysis applications, instead of the conventional 2D raft-like Pt and Ru NPs that are obtained on γ-Al_2O_3 through deposition-precipitation.[15,17] This suggests that the cluster-support interactions that are thought to influence the dispersion and shape of nanoscale Pt catalysts[26] on Al_2O_3 may be tuned by changing the sample preparation method.

2. Experimental Methods

2.1. Sample Preparation. Size-selected Pt NPs were chemically synthesized by inverse micelle encapsulation. The dissolution of nonpolar/polar diblock copolymers [Poly(styrene)-block-poly-(2vinylpyridine), Polymer Source Inc.] in a nonpolar solvent (toluene) leads to the formation of spherical nanocages known as reverse micelles. Size-selected Pt NPs are formed when the former polymeric solution is loaded with $H_2PtCl_6 \cdot 6H_2O$. In these samples, the particle size was changed by using two polymers with different head lengths (P2VP group), namely, PS(27700)-P2VP(4300) (sample S1) and PS(16000)-P2VP(3500) (samples S2, S3, S4, S5), as well as by modifying the metal-salt/polymer-head (P2VP) ratio (L). The following L ratios were used in the present study: 0.05 (S2), 0.1 (S3), 0.2 (S1, S4), and 0.4 (S5). Two sets of analogous samples were prepared using these micellar-NP solutions; one set supported on nanocrystalline γ-Al_2O_3 powder (∼40 nm) for EXAFS and TEM measurements/analysis (Table 1), and a second, analogous set supported on single crystals [SiO_2/Si(100) and TiO_2(110)] for AFM and STM measurement/analysis (Table 2). The second set was made to obtain complementary height information since TEM only gives information about the diameter of our particles, and our powder samples are not AFM/STM compatible. Further sample preparation details can be found in Tables 1, 2, and refs 23−25, 27. The metal−polymeric solutions for the EXAFS/TEM samples were mixed with the γ-Al_2O_3 powder resulting in a loading of 2 wt % (S1) and 1 wt.% (S2, S3, S4, S5) Pt. The samples were stir-dried in air at ∼60 °C for 24 h, and subsequently calcined in O_2 at 375−425 °C for 24 h for the removal of the encapsulating polymer. The total gas flow during calcination in a packed-bed reactor was 50 mL/min, with 50−70% O_2 balanced by He. The process for polymer removal from the NPs deposited on single crystals [SiO_2/

(9) Giorgio, S.; Cabie, M.; Henry, C. R. *Gold Bull.* **2008**, *41*, 167.

(10) Giorgio, S.; Sao Joao, S.; Nitsche, S.; Chaudenson, D.; Sitja, G.; Henry, C. R. *Ultramicroscopy* **2006**, *106*, 503.

(11) Wang, Q.; Hanson, J. C.; Frenkel, A. I. *J. Chem. Phys.* **2008**, *129*, 234502.

(12) Helveg, S.; Hansen, P. L. *Catal. Today* **2006**, *111*, 68.

(13) Newton, M. A. *Chem. Soc. Rev.* **2008**, *37*, 2644.

(14) Newton, M. A.; Belver-Coldeira, C.; Martinez-Arias, A.; Fernandez-Garcia, M. *Nat. Mater.* **2007**, *6*, 528.

(15) Karim, A.; Prasad, V.; Mpourmpakis, G.; Lonergan, W. W.; Frenkel, A. I.; Chen, J. G.; Vlachos, D. G. *J. Am. Chem. Soc.* **2009**, *131*, 12230.

(16) Frenkel, A. I.; Hills, C. W.; Nuzzo, R. G. *J. Phys. Chem. B* **2001**, *105*, 12689.

(17) Sanchez, S. I.; Menard, L. D.; Bram, A.; Kang, J. H.; Small, M. W.; Nuzzo, R. G.; Frenkel, A. I. *J. Am. Chem. Soc.* **2009**, *131*, 7040.

(18) Knecht, M. R.; Weir, M. G.; Frenkel, A. I.; Crooks, R. M. *Chem. Mater.* **2008**, *20*, 1019.

(19) Li, Z. Y.; Young, N. P.; Di Vece, M.; Palomba, S.; Palmer, R. E.; Bleloch, A. L.; Curley, B. C.; Johnson, R. L.; Jiang, J.; Yuan, J. *Nature* **2008**, *451*, 46.

(20) Huang, W. M.; Sun, R.; Tao, J.; Menard, L. D.; Nuzzo, R. G.; Zuo, J. M. *Nat. Mater.* **2008**, *7*, 308.

(21) Frenkel, A. I. *Z. Kristallogr.* **2007**, *222*, 605.

(22) Frenkel, A. I. *J. Synchrotron Radiat.* **1999**, *6*, 293.

(23) Ono, L. K.; Sudfeld, D.; Roldan Cuenya, B. *Surf. Sci.* **2006**, *600*, 5041.

(24) Naitabdi, A.; Ono, L. K.; Behafarid, F.; Roldan Cuenya, B. *J. Phys. Chem. C* **2009**, *113*, 1433.

(25) Naitabdi, A.; Behafarid, F.; Roldan Cuenya, B. *Appl. Phys. Lett.* **2009**, *94*, 083112.

(26) Nellist, P. D.; Pennycook, S. J. *Science* **1996**, *274*, 413.

(27) Croy, J. R.; Mostafa, S.; Heinrich, H.; Roldan Cuenya, B. *Catal. Lett.* **2009**, *131*, 21.

Table 1. Description of Synthesis Parameters and Size (TEM) Information of Micellar Pt NPs Supported on Nanocrystalline γ-$Al_2O_3{}^a$

	synthesis details of the "as-prepared" Pt NPs/γ-Al_2O_3			TEM analysis after annealing + XAFS measurements in H_2 at 375 °C	
sample name	polymer	L	annealing T (°C) [(% O_2)]	TEM diameter (nm)	TEM weighted diameter (nm)
S1	PS(27700)-P2VP(4300)	0.2	375 [50]	1.0 (0.2)	1.2 (0.2)
S2	PS(16000)-P2VP(3500)	0.05	375 [50]	1.0 (0.2)	1.1 (0.2)
S3	PS(16000)-P2VP(3500)	0.1	425 [70]	1.0 (0.2)	1.2 (0.3)
S4	PS(16000)-P2VP(3500)	0.2	400 [50]	0.9 (0.2)	1.0 (0.2)
S5	PS(16000)-P2VP(3500)	0.4	375 [50]	1.7 (1.5)	5.7 (2.2)

^{a} The TEM values correspond to NP diameters. The volume-weighted TEM diameters are also indicated. The parameter "L" represents the metal-salt to polymer ratio used in the NP synthesis.

Table 2. Height Analysis of Pt NPs Supported on SiO$_2$/Si(100) (AFM) and TiO$_2$(110) (STM)^a

	complementary size analysis	
analogous sample	AFM height (nm) after RT O_2-plasma (UHV)	STM height (nm) after RT O_2-plasma + UHV annealing (°C)
S1	1.2 (0.5)	1.8 (0.4) (500 °C)
S2		0.9 (0.3) (1000 °C)
S3		1.0 (0.3) (500 °C)
S4		1.3 (0.3) (500 °C)
		1.3 (0.4) (900 °C)
S5	1.1 (0.4)	1.5 (0.4) (500 °C)
		1.5 (0.4) (700 °C)

^{a} The AFM and STM values correspond to the NP heights measured at RT after polymer removal by an O_2-plasma treatment at RT (AFM), and after subsequent annealing in UHV at 500°C (S1, S3, S4), 900°C (S4), and 1000°C (S2) (STM).

Si(100) and TiO$_2$(110)] used in the AFM/STM measurements involved an O_2-plasma treatment in UHV at room temperature (RT) (4.0×10^{-5} mbar for 2 h).

2.2. Sample Characterization. The AFM/STM NP solutions were dip-coated onto SiO$_2$/Si(100) and TiO$_2$(110) substrates for morphological characterization by ex situ atomic force microscopy (AFM, Digital Instruments-Nanoscope III) and in situ scanning tunneling microscopy (STM, SPECS-Aarhus), respectively (Table 2). The AFM images were taken after polymer removal in ultrahigh vacuum (UHV) by an O_2-plasma treatment. The SiO$_2$/Si(100) substrate was chosen for AFM measurements because of its low surface roughness (~0.2 nm), while STM measurements require a conducting substrate; therefore, TiO$_2$(110) was used. Furthermore, after UHV treatments and subsequent air exposure, the TiO$_2$ substrate becomes too rough for reliable AFM measurements considering our small particle sizes. Thus, AFM measurements were not carried out on the TiO$_2$ substrates. The STM samples were measured in UHV after atomic oxygen exposure and annealing in order to minimize artifacts arising from the enhanced TiO$_2$ roughness that resulted from the in situ O_2-plasma treatment as well as to improve the tunneling conditions. The annealed TiO$_2$ substrates are partially reduced and therefore more conducting, facilitating thus the STM measurements.

TEM samples were prepared by making an ethanol suspension of the Pt/γ-Al$_2$O$_3$ powder, after EXAFS measurements, by placing a few drops of this liquid onto an ultrathin C grid, and allowing the sample to air-dry. High-angle annular dark-field (HAADF) images of the Pt/γ-Al$_2$O$_3$ samples were acquired under scanning mode within a JEM 2100F TEM, operated at 200 kV. The probe size of the STEM is about 0.2 nm. The Pt NP diameters were determined by measuring the full width at half-maximum of the HAADF intensity profile across the individual Pt NPs (Table 1).

X-ray photoelectron spectroscopy (XPS) measurements were carried out on each powder sample before the XAFS measurements to monitor the removal of the encapsulating polymer (C-1s signal) as well as any possible Cl residues (Cl-2p) from the NP synthesis (see Supplemental Figure 1). No contaminants were detected on these samples after the calcination treatment in O_2 described above. The XPS data were collected in UHV using a monochromatic X-ray

source (Al Kα, 1486.6 eV, SPECS GmbH) operating at 250 W. A flood gun was used during measurements to correct for sample charging. All spectra were referenced to the Al-2s peak in Al$_2$O$_3$ at 119.2 eV.

XAFS measurements were carried out at beamline X18B at the National Synchrotron Light Source (NSLS) at Brookhaven National Laboratory (Upton, NY). The data were collected in transmission mode using the Pt L$_3$ edge. The XAFS samples were prepared by pressing the Pt/γ-Al$_2$O$_3$ powders into thin pellets which were mounted in a sample cell that permitted sample heating via an external PID controller, liquid nitrogen cooling, as well as the continuous flow of gases during data acquisition and their online mass spectrometer analysis.[16] A bulk Pt foil was measured in transmission simultaneously with all samples for energy calibration purposes. The EXAFS data were collected at RT in He (as-prepared) and after annealing/reduction at 375 °C in 50% H$_2$ balanced with He for a total flow rate of 50 mL/min. EXAFS data from the reduced samples where acquired at temperatures ranging from -100 to 375 °C in 50% H$_2$ (50 mL/min, He balance) under the same gas flow conditions. Multiple scans (up to 6) were collected at each temperature of interest and averaged in order to improve signal-to-noise ratios.

3. Data Analysis

3.1. EXAFS. Data processing and analysis was done using the Athena and Artemis software[28] from the IFEFFIT package.[29] EXAFS data in k-space were obtained from raw absorption coefficient data by subtracting a smooth, isolated-atom background by the AUTOBK method.[30] The FEFF6 code[31] was used to construct theoretical EXAFS signals that included single- and multiple-scattering contributions from atomic shells through the fourth nearest neighbors in the face-centered cubic (fcc) structure of Pt. To minimize the temperature-dependent bond length disorder contributions, such multiple-scattering analysis was done only for the low temperature (-85 to -108 °C and RT) data. The typical k-range used in the fitting was from 2.5 to 19 Å^{-1}, and the r-range from 1.7 to 5.7 Å. Thus, the total number of relevant independent data points in the analysis ($N_{idp} = 2\Delta k \Delta r/\pi$)[32] was of the order of 40, depending on the sample, while the number of variables in the fit was much smaller, namely, 13. To extract local structural information from the reduced samples, we constructed theoretical EXAFS signals from the contributions of the most important photoelectron propagators (paths) for the fcc structure. They are the following: single scattering (SS) paths to the first four nearest neighbors, x → 1NN → x, x → 2NN → x, x → 3NN → x, x → 4NN →

(28) Ravel, B.; Newville, M. *J. Synchrotron Radiat.* **2005**, *12*, 537.
(29) Newville, M. *J. Synchrotron Radiat.* **2001**, *8*, 322.
(30) Newville, M.; Livins, P.; Yacoby, Y.; Rehr, J. J.; Stern, E. A. *Phys. Rev. B* **1993**, *47*, 14126.
(31) Zabinsky, S. I.; Rehr, J. J.; Ankundinov, A.; Albers, R. C.; Eller, M. J. *Phys. Rev. B* **1995**, *52*, 2995.
(32) Brillouin, L. *Science and Information Theory*; Academic Press: New York, 1962.

x (where x denotes the X-ray absorbing atom); double scattering focusing (DSF) paths, including the time-reversed ones, to the 4NN through the intervening 1NN, x → 1NN → 4NN → x; triple-scattering focusing (TSF) paths corresponding to the same group of neighbors, except for the forward scattering through the intervening atom twice (x → 1NN → 4NN → 1NN → x); and, finally, the triple-scattering focusing paths from the central atom to its 1NN on each side (1NN and 1NN*), x → 1NN → x → 1NN* → x. This path selection is similar to that described in the previous works analyzing high order contributions to fcc NPs.[16,22,33] Each path degeneracy was allowed to vary in the fit to account for size effects that cause surface atoms to be less coordinated than those in the particle interior. Constraints between coordination numbers were set to follow ref 22. The DSF and TSF paths to the 4NN had their mean square disorder parameters constrained to be the same as that of the SS path to the same neighbors.[34] Finally, the nearest neighbor distances, except for the 1NN, were constrained to follow the isotropic bond distortion model, maintaining the overall fcc symmetry. This assumption is validated later by the high crystalline order obtained in the reduced NPs, *vide infra*. The passive electron reduction factor (S_0^2) was fixed to 0.861, as obtained from the multiple-scattering fitting analysis of the bulk Pt foil. The correction to the photoelectron energy origin was varied in the fit, and was kept the same for all paths. We have also included the third cumulant of the 1NN pair distribution function. The latter parameter was not found to affect the results of the fits significantly (since we analyzed the data collected at relatively low temperatures where that parameter is not significant), and the final results are shown without accounting for the third cumulant. The same model was applied to the analysis of the bulk Pt data for calibration, and the results obtained were found to be in good agreement with its known coordination numbers and NN distances. For the as-prepared samples, we constructed the fitting model by accounting for the Pt−O contribution that is evident in the raw data. That contribution was modeled by FEFF6 calculations done for the crystal structure of $Na_2Pt(OH)_6$. In addition to Pt−O, only 1NN Pt−Pt contributions were included in the analysis. The total number of relevant independent data points was 13, which is much larger than the total number of fitting variables (7).

3.2. Nanoparticle Shape Modeling. A MATLAB code was written to obtain coordination numbers corresponding to different Pt NP shapes with fcc structure. A shape database was generated starting from a bulk fcc structure that was subsequently truncated along two different planes, {111} (8 facets) and {100} (6 facets). Higher Miller index facets have not been considered, since they are energetically less favorable and have not been observed in previous high resolution STM and TEM studies of particles within the same size range.[35−39] Distinct NP shapes were obtained by changing the distance of each of the above facets to the center of the NP. The resultant database

(33) Nashner, M. S.; Frenkel, A. I.; Adler, D. L.; Shapley, J. R.; Nuzzo, R. G. *J. Am. Chem. Soc.* **1997**, *119*, 7760.

(34) Shanthakumar, P.; Balasubramanian, M.; Pease, D.; Frenkel, A. I.; Potrepka, D.; Budnick, J.; Hines, W. A.; Kraizman, V. *Phys. Rev. B* **2006**, *74*, 174106.

(35) Dulub, O.; Hebenstreit, W.; Diebold, U. *Phys. Rev. Lett.* **2000**, *84*, 3646.

(36) Berko, A.; Szoko, J.; Solymosi, F. *Surf. Sci.* **2003**, *532−535*, 390.

(37) Ramachandran, A. S.; Anderson, S. L.; Datye, A. K. *Ultramicroscopy* **1993**, *51*, 282.

(38) Giorgio, S.; Henry, C. R.; Chapon, C. *J. Cryst. Growth* **1990**, *100*, 254.

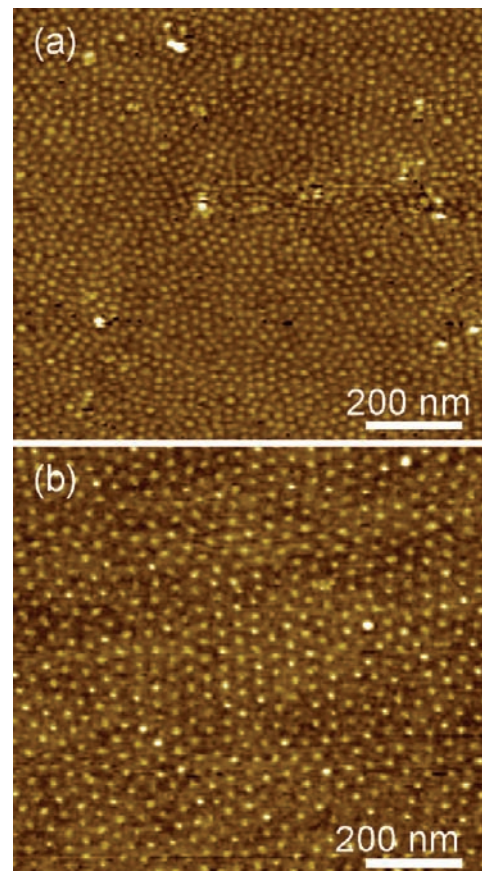(39) Graoui, H.; Giorgio, S.; Henry, C. R. *Surf. Sci.* **1998**, *417*, 350.

Figure 1. AFM images of micellar Pt NPs supported on $SiO_2/Si(100)$ taken ex situ after polymer removal by an O_2-plasma treatment. The samples were synthesized with the same NP solutions used for the EXAFS characterization. Image (a) corresponds to NPs synthesized by encapsulation with PS(16000)-P2VP(3500) (analogous to S5) and (b) on PS(27700)-P2VP(4300) (analogous to S1).

includes octahedron, cuboctahedron, truncated octahedron, and hexahedron shapes, as well as combinations of the above (mixed shapes). In a second step, the symmetric shapes previously described were truncated (layer-by-layer) following (111) and (100) facets. In total, we have considered 131 symmetric shapes, 1643 shapes truncated along (111), and 1715 shapes truncated along (100) facets. Hexahedron (cubic) shapes have not been included in the subsequent analysis since such shapes were not previously observed for analogously prepared but larger (∼3 nm) Pt NPs via STM. For each of the remaining shapes, the NP height, diameter, total number of atoms, and average nearest neighbor coordination numbers (N1−N4) were calculated and compared to the experimental values obtained by EXAFS (coordination numbers) and TEM (NP diameter). Some preliminary analysis was also done for the cubic shapes, but none of them were found to lead to a better agreement with the EXAFS coordination numbers than the noncubic shapes reported in the subsequent sections.

4. Results

4.1. Morphological and Structural Characterization (AFM, STM, STEM). Figure 1 shows AFM images of samples prepared with NP solutions analogous to the XAFS samples S5 (a) and S1 (b) but supported on $SiO_2/Si(100)$ taken after the removal of the polymeric shell by an in situ O_2-plasma at RT, which leaves the NPs highly oxidized (see XPS data of Supplemental
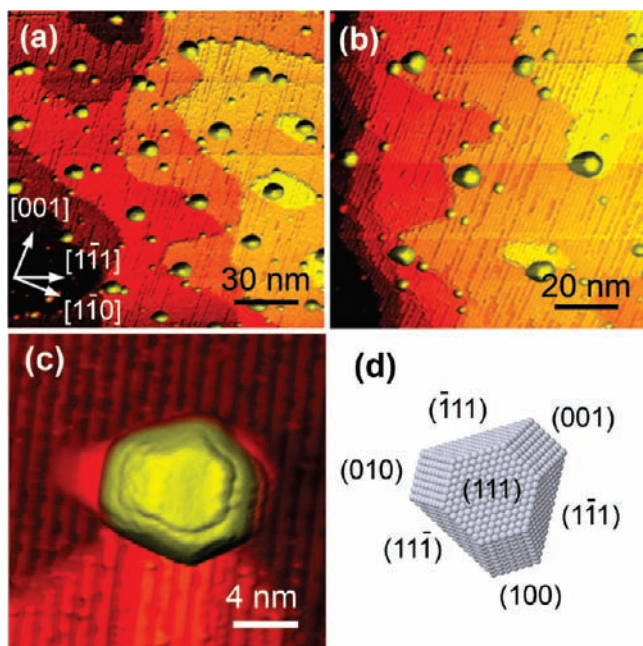
Figure 2. (a and b) STM images of micellar Pt NPs on TiO₂(110) after polymer removal by an O₂-plasma treatment and subsequent annealing in UHV at 900 °C. The NP solution used to prepare this sample is similar to that of sample S1. Image (c) shows the shape resolved STM image of a faceted micellar NP prepared using the polymer PS(81000)-P2VP(14200). Image (d) shows the facet orientations of an atomic model of a particle constructed based on an fcc crystalline structure.

Figure 2). Narrow NP size distributions are observed for both samples, with average NP heights of ∼1.2 and ∼1.1 nm, respectively (see Supplemental Figure 3). The use of two polymers with distinct tail lengths in the synthesis leads to two different average interparticle distances, namely, ∼36 nm (S5) and ∼43 nm (S1). Since in this NP size range ex situ AFM characterization is challenging, our morphological analysis was complemented by in situ STM measurements on similar NP solutions dip-coated on TiO₂(110). STM images were acquired after polymer removal by atomic oxygen exposure and subsequent sample annealing in ultrahigh vacuum at 500 °C (30 min) and 900 °C (20 min), which also reduces any oxides from the plasma treatment (Supplemental Figure 2). Figure 2 displays examples of STM images acquired on the micellar Pt NPs of sample S1 after annealing at 900 °C. For a given sample, no clear changes in the STM NP height were observed when comparing samples annealed at 500, 700, 900, and 1000 °C, indicating the lack of NP coarsening and/or atomic desorption. In this sample, the average NP height at 900 °C was 1.8 ± 0.4 nm. We mention that, even though the AFM-measured (air exposed) samples were not reduced (i.e., not annealed), and contain an oxide shell as evidence by XPS (see Supplemental Figure 2), good agreement is observed between the NP heights obtained by AFM (oxidized) and STM (reduced), Table 2. Therefore, we assume that the presence of oxides does not influence the AFM size within the errors given. It is possible that due to the single crystal supports being different than our γ-Al₂O₃ support the AFM/STM heights may not be representative of the height of the NPs analyzed by EXAFS. However, because these two different methods (AFM/STM) give similar results under differing conditions (unannealed/UHV-annealed and on two different supports), we believe the measurements to be reasonable representatives for the 3D-shaped γ-Al₂O₃-supported NPs (S1, S3, S4, S5). S2 is an exception to this

general trend, since its 2D nature is attributed at least partially to a strong NP/support interaction (Pt/γ-Al₂O₃) that might not be present on the other two supports. The differences observed for S1 are due to the fact that two different NP solutions (of similar characteristics) were used to prepare each sample. Histograms of the STM heights can be found in Supplemental Figure 4.

Figure 3 displays examples of HAADF-STEM images obtained for micellar Pt NPs supported on nanocrystalline γ-Al₂O₃. The HAADF images correspond to samples S1 (a) and 2 (b) and were acquired after polymer removal by a prolonged annealing in O₂ at 375 °C and subsequent in situ XAFS characterization after reduction in H₂ at 375 °C. Histograms of the Pt NP diameters as measured from the HAADF images are included in Figure 3, panels c (300 NP count) and d (602 NP count), respectively. Size histograms extracted from HAADF measurements of the rest of the samples discussed in this manuscript can be found in Supplemental Figure 5 and the average diameters in Table 1. With the exception of sample S5, where coarsening seems to have occurred during the polymer removal pretreatment leading to a certain population of large NPs, the rest of the samples are characterized by narrow NP size distributions with NPs smaller than 1.5 nm.

4.2. Structural, Electronic, and Chemical Characterization (XANES, EXAFS). Figure 4 shows X-ray absorption near-edge structure (XANES) spectra of the Pt L₃ edge of the micellar Pt NPs supported on γ-Al₂O₃ acquired (a) before and (b) after in situ reduction in H₂ at 375 °C. Reference data obtained on a Pt foil are also displayed. The resonance peak at the absorption edge is known as the white line (WL) and it arises from 2p₃/₂ to 5d₅/₂, 5d₃/₂ transitions. The intensity of the WL increases with decreasing d-band occupancy, and it is very strong for transition metals with a partially filled d band (e.g., Pt-5d₅/₂ orbital). The area under the WL can be used to extract information on d-charge redistributions.[40] The spectra in Figure 4a reveal the strongly oxidized character of the as-prepared Pt NPs samples. The WL intensities of the former samples are significantly higher than those of the reduced samples, Figure 4b, due to the electron-withdrawing nature of oxygen. This result is in agreement with EXAFS data acquired for the same samples and will be discussed in greater detail below. Furthermore, a size-dependence in the WL intensity is observed, with the lowest value measured for the largest NPs (S5, 1.7 ± 1.5 nm), followed by the 0.9−1.0 ± 0.2 nm NPs (S3, S4). Surprisingly, similarly sized NPs in S2 (1.0 ± 0.2 nm) showed a clearly higher WL intensity. The more facile oxidation of small metal NPs can explain the differences between samples S5 and S3, S4, but not the higher WL intensity of S2. We will elaborate on this point in the discussion section.

After NP reduction in H₂, the WL intensity of all NP samples is significantly decreased, reaching the bulk-Pt value. In agreement with previous reports,[41−48] we also observe the shift

(40) Prins, R.; Koningsberger, D. C. In *X-ray Absorption. Principles, Applications, Techniques of EXAFS, SEXAFS, and XANES*; Prins, R., Ed.; Wiley: New York, 1988; Chapter 8.
(41) Vaarkamp, M.; Miller, J. T.; Modica, F. S.; Lane, G. S.; Koningsberger, D. C. *Jpn. J. Appl. Phys.* **1993**, *32*, 454.
(42) Lytle, F. W.; Gregor, R. B.; Marques, E. C.; Sandstrom, D. R.; Via, G. H.; Sinfelt, J. H. *J. Catal.* **1985**, *95*, 546.
(43) Samant, M. G.; Boudart, M. *J. Phys. Chem. B* **1991**, *95*, 4070.
(44) Ichikuni, N.; Iwasawa, Y. *Catal. Lett.* **1993**, *20*, 87.
(45) Allen, P. G.; Conradson, S. D.; Wilson, M. S.; Gottesfeld, S.; Raistrick, I. D.; Valerio, J.; Lovato, M. *Electrochim. Acta* **1994**, *39*, 2415.
(46) Asakura, K.; Kubota, T.; Chun, W. J.; Iwasawa, Y.; Ohtani, K.; Fujikawa, T. *J. Synchrotron Radiat.* **1999**, *6*, 439.
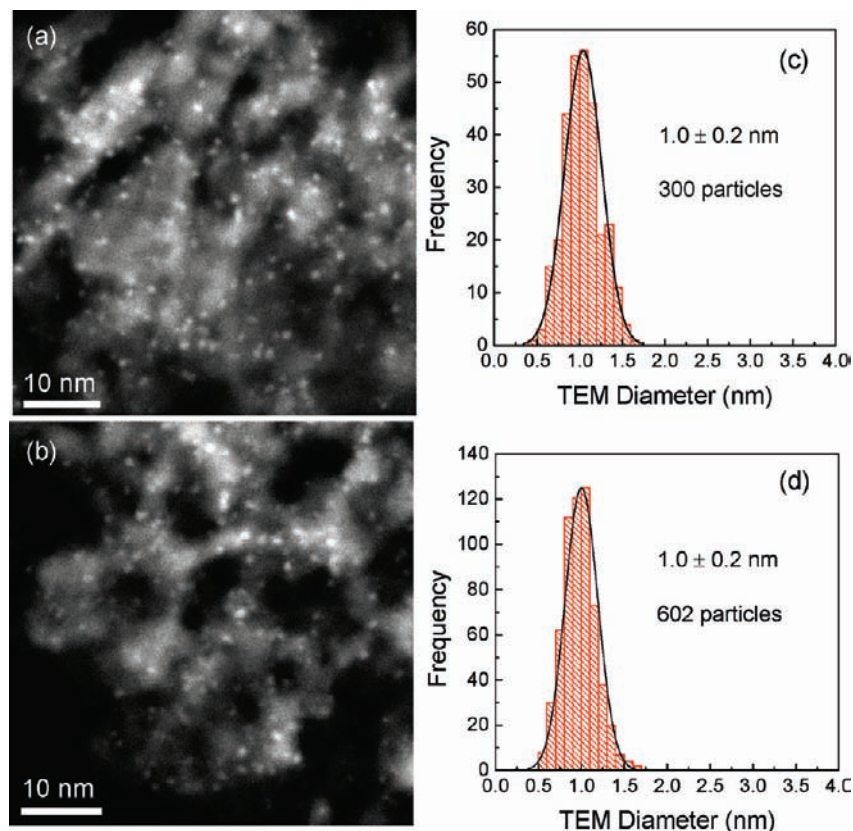(47) Kubota, T.; Asakura, K.; Ichikuni, N.; Iwasawa, Y. *Chem. Phys. Lett.* **1996**, *256*, 445.

Figure 3. HAADF STEM images of micellar Pt NPs on γ-Al$_2$O$_3$: (a) S1, and (b) S2. The images were taken after polymer removal by annealing in O$_2$ at 375 °C. Histograms of the corresponding NP diameter distributions are shown in panels c and d.

of the peak position to higher energies (relative to the bulk), and the overall peak broadening for all NP samples. The origins of these effects are subjects of intense debate in the literature.[43,44,46,49−55] The blue shift of the WL observed for the NP samples relative to the Pt foil [inset in Figure 4b] is most noticeable for S2 (+1.2 eV) but also present for the other samples (+0.5 eV for S1). We note here that the setup at beamline X18B along with our calibration procedures allow us to discern relative energy shifts with a sensitivity better than 0.1 eV.

Figure 5 displays k^2-weighted EXAFS data in k-space (a) and r-space (b) acquired at RT in H$_2$ for all reduced samples. A comparison with the data obtained for the oxidized (as-prepared) samples at RT in He is shown in the inset of Figure 5b. For NPs of identical shape, the amplitudes of the EXAFS oscillations in Figure 5a are related to distinct values of average NP size and bond length disorder, with small (<5 nm) and most disordered NPs showing significantly damped signals. For our samples, S5 appears to contain large NPs (similar signal to the
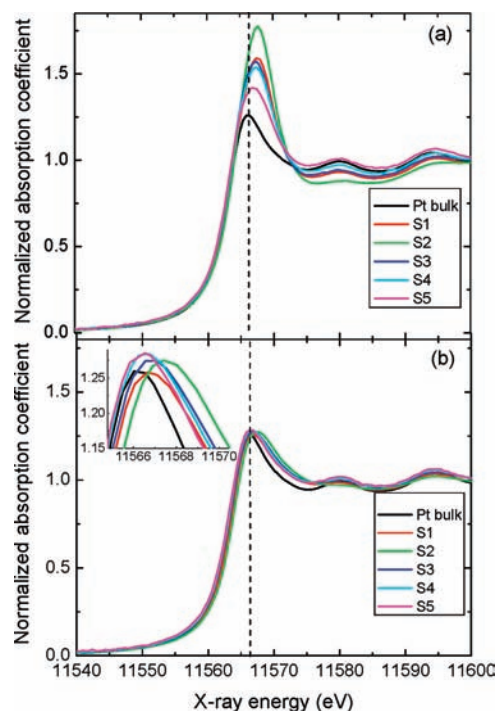
(48) Yoshitake, H.; Mochizuki, T.; Yamazaki, O.; Ota, K. *J. Electroanal. Chem.* **1993**, *361*, 229.
(49) Vaarkamp, M.; Modica, F. S.; Miller, J. T.; Koningsberger, D. C. *J. Catal.* **1993**, *144*, 611.
(50) Otten, M. M.; Clayton, M. J.; Lamb, H. H. *J. Catal.* **1994**, *149*, 211.
(51) Vaarkamp, M.; Mojet, B. L.; Kappers, M. J.; Miller, J. T.; Koningsberger, D. C. *J. Phys. Chem. B* **1995**, *99*, 16067.
(52) Ankudinov, A. L.; Rehr, J. J.; Low, J. J.; Bare, S. R. *J. Synchrotron Radiat.* **2001**, *8*, 578.
(53) Ankudinov, A. L.; Rehr, J. J.; Low, J. J.; Bare, S. R. *Top. Catal.* **2002**, *18*, 3.
(54) Soldatov, A. V.; Della Longa, S.; Bianconi, A. *Solid State Commun.* **1993**, *85*, 863.
(55) Matsuura, A. T.; Fujikawa, T.; Kuroda, H. *J. Phys. Soc. Jpn.* **1983**, *52*, 3275.
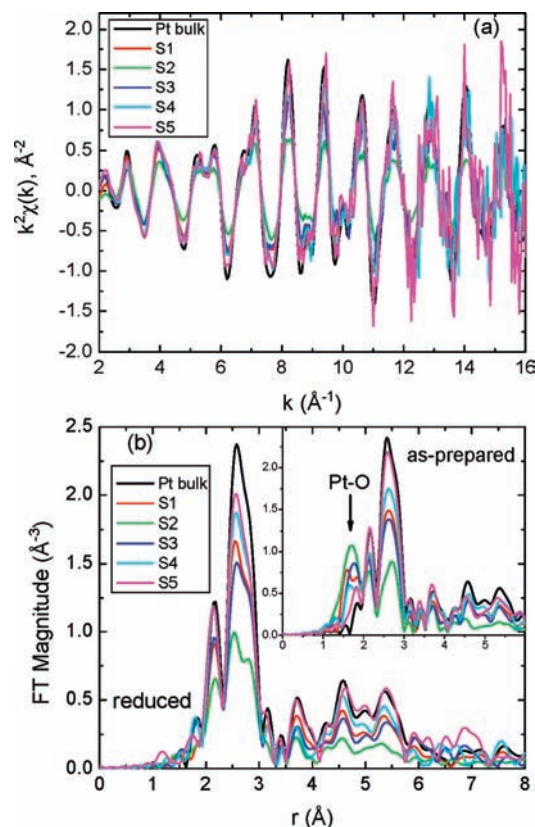
Figure 4. XANES region [$\mu(E)$ versus E] of (a) oxidized "as-prepared" micellar Pt/γ-Al$_2$O$_3$ samples at RT in He, and (b) reduced samples at RT in H$_2$ measured after annealing in H$_2$ at 375 °C. Similar data from a Pt foil are also displayed. The inset in panel b shows a positive shift in the energy of the Pt L$_3$ edge of Pt NPs as compared to the bulk Pt reference.

bulk Pt foil), while the EXAFS data from sample S2 indicate the smallest and/or most atomically disordered NPs among all

Figure 5. k^2-weighted EXAFS data in k-space (a) and r-space (b) for all reduced samples in H_2 at room temperature. The inset in panel b shows data from the as-prepared samples measured in He at RT. Fourier transform parameters are as follows: the k-range is from 2 to 16 Å^{-1}, the Hanning window sills are $\Delta k = 2$ Å^{-1}.

samples. The same trend is observed in the r-space data of Figure 5b. We point out here that, as discussed previously, the coordination numbers of the 1NNs do not provide conclusive information on the NP size, since many clusters of different shapes and sizes may have the same 1NN coordination number.[56] Furthermore, visual examination of the data does not allow one to easily discriminate among the individual effects of size, shape, and atomic disorder. In this work, we use multiple-scattering fitting analysis to extract first through fourth coordination numbers for the quantitative analysis of NP shapes. Details in this respect will be given in the next section. The inset in Figure 5b reveals a strong Pt–O peak in the as-prepared (oxidized) samples measured in He. Interestingly, almost all of the as-prepared samples (with the exception of sample S2) display a well-ordered fcc structure. The highest Pt–O signal and highest atomic disorder were observed for sample S2. We would like to highlight that PtO cannot be distinguished from PtO$_2$ based on EXAFS signals of the first shell, since the Pt–O distances for both species are about 2 Å (2.04 Å for PtO and 1.99 Å for β-PtO$_2$).[57] Nevertheless, from our EXAFS data, we can conclude, by analysis of the coordination numbers of Pt–O and Pt–Pt, that the "as-prepared" Pt/γ-Al$_2$O$_3$ samples contained a maximum of ~65% PtOx and ~35% metallic Pt (data obtained from S2 reflecting the maximum relative content of Pt–O species among all of our samples).

5. Discussion

As was mentioned in the previous section, the unusually high WL intensity of S2 as compared to samples S3 and S4 [Figure 4a, as-prepared samples] cannot be understood simply based on the stronger degree of oxidation of smaller NPs, since all three samples were found to contain relatively monodispersed ~1 nm (diameter) NPs according to TEM. Instead, we attribute the enhanced density of unoccupied 5d states in S2 to a distinct shape of the NPs in this sample, namely, a flatter geometry with the same apparent TEM diameter but an enhanced NP/support contact area. Indeed, such model is consistent with the enhanced WL intensity, since XANES data contain ensemble-averaged information about the density of unoccupied Pt-5d states. Thus, the greater the fraction of Pt atoms with a large 5d-hole density (i.e., those which are oxidized, for example via support interaction), the larger the WL intensity. This model is also consistent with the TEM-obtained average NP diameter. One possible explanation for the WL enhancement of the Pt atoms at the NP–substrate interface is the large charge transfer from Pt to defects in Al$_2$O$_3$.[58] The inset in Figure 5b, displaying r-space EXAFS data from the as-prepared oxidized samples, also reveals the highest Pt–O signal for sample S2, consistent with the XANES observation.

A comparison of the r-space plots shown in Figure 5b for the reduced micellar Pt NPs to that of a bulk Pt foil revealed that despite their small size (~1 nm for most samples), all of our NPs have good crystalline fcc structure, in contrast with previous literature reports on similarly sized NPs prepared by deposition-precipitation methods.[17] This difference could be attributed to several factors: (i) the reverse micelle encapsulation method leads to more ordered structures, (ii) the prolonged annealing times (24 h) used during the pretreatment of the micellar NP samples (before XAFS characterization) lead to an enhanced long-range order, and (iii) the shape of most of our NPs (S1, 3, 4 and 5) is 3D, instead of raft-like (2D) as has been commonly reported for Pt/γ-Al$_2$O$_3$.[17] In the latter case, strain from the larger NP/support contact area is expected to lead to more disordered structures. In addition, it should be noted that our XAFS measurements were carried out in a H$_2$ atmosphere, and that H$_2$ has been reported to induce faceting on NPs.[9,10] Sanchez et al.[17] also suggested, by comparing EXAFS results from Pt/C and Pt/γ-Al$_2$O$_3$ measured under He and H$_2$ flows, that H$_2$ relieves surface-induced strain. Wang and Johnson[59] have interpreted those results theoretically by attributing the increased order in the clusters to removal of the inherent {100}-to-{111} shear instability, stabilizing the truncated cubocathedral shape when the particles are passivated by hydrogen. If the micellar NPs are 3D in nature, a higher surface area is available for H$_2$ absorption, and therefore, more ordered faceted NPs will be present. Interestingly, sample S2 shows the least resemblance to the Pt foil, and since the diameter of the NPs in this sample is nearly identical to that in sample S1, qualitatively, a more anisotropic shape might be inferred for sample S2.

The EXAFS data from Figure 5 (RT measurements) as well as low-temperature (−85 to −100 °C) data have been fit by multiple scattering analysis. The excellent quality of the fits obtained for two representative samples (S1 and S2) is demonstrated in Figure 6. From these fits, coordination numbers

(56) Glasner, D.; Frenkel, A. I. *AIP Conf. Proc.* **2007**, *882*, 746.
(57) Seriani, N.; Jin, Z.; Pompe, W.; Ciacchi, L. C. *Phys. Rev. B* **2007**, *76*, 155421.
(58) Kwak, J. H.; Hu, J.; Mei, D.; Yi, C.-W.; Kim, D. H.; Peden, C. H. F.; Allard, L. F.; Szanyi, J. *Science* **2009**, *325*, 1670.
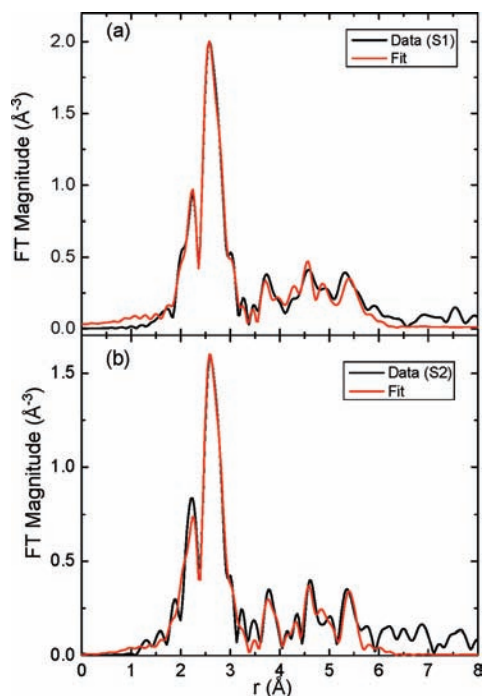(59) Wang, L. L.; Johnson, D. D. *J. Am. Chem. Soc.* **2007**, *129*, 3658.

Figure 6. Fourier transform magnitudes of the k^2-weighted EXAFS data and multiple-scattering fit for the sample S1 measured at room temperature (a) and sample S2 measured at −85 °C (b).

of, and distances to, the first through the fourth nearest neighbor shells have been extracted, Table 3, and used to gain information on the NP shape by comparison with model fcc cluster shapes, Figure 7. In Table 3, N1, N2, N3, and N4 represent the coordination numbers of Pt−Pt coordination shells that correspond to the first through the fourth nearest neighbors in the fcc structure. The distances (r) to each of these neighboring shells are also shown in Table 3. Frenkel et al.[16] have previously used the sequence of nearest neighbor atomic distances and coordination numbers extracted from EXAFS measurements to correlate different models for cluster shapes with average cluster diameters obtained independently. In the present study, the synergistic combination of the EXAFS multiple scattering analysis, NP size information obtained by TEM, and calculations of model clusters shapes has revealed the 3D cluster shape of NPs in samples S1, S3, S4 and S5, and 2D raft-like NP shapes for sample S2. The final NP shape determination is based on the best agreement between EXAFS-obtained coordination numbers and those derived for a particular model fcc Pt cluster shape that would be in the size range indicated by our TEM data. However, it should be mentioned that such analysis is only meaningful if samples with narrow size distributions are available (S1, S2, S3, S4), since only then will it be possible to reduce the number of model cluster shapes that agree with the EXAFS coordination numbers as well as TEM NP diameters. In addition, the NP size should be small (<ca. 3 nm), since a large degeneracy in shapes is otherwise obtained when coordination numbers close to the bulk fcc metal are considered. Even if all of these requirements are met, additional compromises might be required, for example, ones that compensate for strong distortions expected in the nanometer-scale clusters due to surface and substrate-induced strain.[60] For example, sample S1 has a size of 1.0 ± 0.2 nm (TEM diameter), and

from our model database, no shape was found to be an exact match with the experimental data. This is a result of our consideration of an extensive set of coordination numbers (N1−N4) when looking for matching shapes (see Supplemental Figure 5 for additional details). Only after taking into consideration "relaxed" error bars of the experimental coordination numbers were six shapes identified as reasonable candidates having closely matching coordination numbers with the EXAFS data. For each N value of each sample, we calculate the difference between the model and the measured (EXAFS) coordination number, normalized by the experimental error, and the maximum value for each sample is the allowed relaxation of the error bars. The best fit will be the one with the lowest value of the allowed relaxation having a diameter in the size range of the TEM measurements. However, of the six different shapes identified for S1, only two were in agreement with the TEM-measured diameter, and the final shape chosen (Figure 7) was the one showing the best agreement with the EXAFS-derived coordination numbers. Similar results were obtained for samples S2−S4, each having similar narrow size distributions as in S1. Additionally, since the coordination numbers extracted from EXAFS data are averaged over all NPs in a particular sample, volume-weighted average size (i.e., TEM-obtained diameter) distributions need to be calculated using the number of atoms in each NP (or volume) as a weighting factor. For samples with narrow size distributions (S1, S2, S3, and S4), the volume-weighted average size is only slightly larger than that of the standard distribution, but in the case of sample S5, where a broad NP size distribution is present, the average NP size was found to be significantly higher, explaining thus the large coordination numbers obtained by EXAFS.

For sample S5, a significant number of large (coarsened) NPs were detected by TEM (see Supplemental Figure 6), leading to a broad volume-weighted NP size distribution and large coordination numbers in EXAFS. Therefore, for this sample, a large number of shapes were found to fit the EXAFS data (within the error margins), and the model shape shown in Figure 7a is displayed only for illustration purposes. For the rest of the samples, the discrimination between different model shapes was much more conclusive, as discussed above, and the following NP shapes were inferred from modeling: an octahedron (S1, S4), cuboctahedron (S3), and a flat (2-layers high) truncated octahedron (S2).[15,61] The most common NP shapes, observed by our group via STM for annealed micellar NPs supported on TiO$_2$(110), were used as reference to discard unstable cluster shapes consisting of nonenergetically favorable facets. Our data analysis indicates the possibility of creating NPs with distinct shapes after annealing (∼400 °C) using the inverse micelle encapsulation method by changing the size of the micellar core (different molecular weight of the P2VP block), as well as by tuning the metal-salt to P2VP ratio (L). In particular, our only 2D shape (S2) was obtained for the lowest loading of the micellar nanocage ($L = 0.05$) considered. More importantly, our results demonstrate that the micelle encapsulation synthesis method allows one to overcome strong NP/support interactions that would normally prevent the stabilization of high-surface area 3D cluster shapes. For NPs in the present size range (∼1 nm), such 3D cluster shapes might display distinct catalytic activity and selectivity as compared to 2D, raft-like Pt/γ-Al$_2$O$_3$ NPs prepared by deposition-precipitation methods due to the larger number of facets in 3D clusters.

(60) Yevick, A.; Frenkel, A. I. *Phys. Rev. B* **2010**, *81*, 115451.

(61) Chang, C. M.; Chou, M. Y. *Phys. Rev. Lett.* **2004**, *93*, 133401.

Table 3. Coordination Numbers (*N*) and Distances of Each Coordination Shell to the Absorbing Atom (*r*) Obtained from the Multiple Scattering Analysis of EXAFS Data Acquired on Micellar Pt NPs Supported on γ-Al$_2$O$_3$[a]

		coordination numbers of the first through the fourth nearest neighbor shells, *N*, and the distance to each shell, *r* (Å)				
	sample	N1 r1	N2 r2	N3 r3	N4 r4	diameter (nm) TEM/model
S1	EXAFS	9.1 (0.5) 2.763(0.004)	2.8 (1.0) 3.910(0.009)	9.8 (2.3) 4.800(0.006)	7.8 (2.0) 5.54(0.01)	1.2 (0.2)
	Model	8.5	3.1	11.3	5.2	1.3
S2	EXAFS	7.3 (0.5) 2.754(0.006)	1.3 (0.7) 3.918(0.004)	5.1 (1.8) 4.799(0.005)	4.4 (1.1) 5.541(0.006)	1.1 (0.2)
	Model	7.0	2.1	7.0	3.1	1.5
S3	EXAFS	8.7 (0.6) 2.758(0.006)	3.4 (1.7) 3.918(0.004)	6.9 (2.3) 4.799(0.005)	5.6 (1.4) 5.541(0.006)	1.2 (0.3)
	Model	7.8	3.3	9.6	4.2	1.3
S4	EXAFS	10.1 (0.6) 2.760(0.005)	5.6 (2.0) 3.918(0.004)	11.8 (3.2) 4.798(0.005)	8.3 (2.2) 5.541(0.006)	1.0 (0.2)
	Model	9.1	3.6	13.4	6.2	1.5
S5	EXAFS	10.9 (1.0) 2.748(0.008)	3.9 (5.6) 3.919(0.006)	14.1 (4.5) 4.800(0.007)	8.5 (2.7) 5.542(0.009)	5.7 (2.2)
	Model	10.6	5.0	18.5	9.2	3.8
Pt bulk	EXAFS	12.0 (0.4) 2.767(0.003)	5.0 (1.2) 3.923(0.003)	24 (4.0) 4.805(0.003)	10.8 (1.6) 5.548(0.004)	thin foil
	Model	12	6	24	12	

[a] The samples underwent an initial annealing as given in Table 1 plus in situ annealing in H$_2$ at 375 °C during XAFS measurements. The fits were carried out on EXAFS spectra measured at low temperature (−85 to −108°C) for samples S2, S3, S4, and S5 and at room temperature for S1. Coordination numbers obtained theoretically for relevant model cluster shapes displayed in Figure 7 are also shown. The model shapes have been selected based on three criteria: (i) their agreement with the coordination numbers extracted by EXAFS, (ii) their agreement with the NP diameters obtained by TEM, and (iii) their resemblance to real cluster shapes observed by STM on similarly synthesized Pt NPs after annealing (see example in Figure 2). The experimental diameters displayed in the EXAFS rows correspond to the average diameters obtained from TEM measurements after volume-weighting the particle diameter histograms. Uncertainties are shown in parentheses.
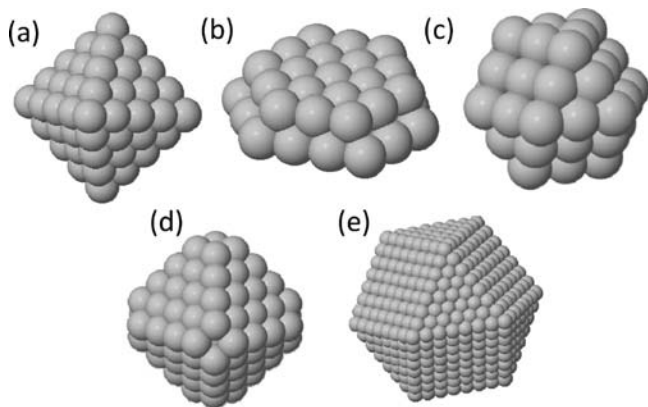

Figure 7. Model of the NP shapes that resulted in the best agreement with the coordination numbers obtained from the fits to the EXAFS data. The shapes are representative of the following samples: (a) S1, (b) S2, (c) S3, (d) S4, and (e) S5. Since a narrow size distribution was not obtained for sample S5, the shape shown in panel e only reflects the volume-weighted size distribution for that sample, since large NPs in that sample will provide the most significant contribution to the observed EXAFS spectra.

Table 4. First Nearest Neighbor (N1) Coordination Numbers of the As-Prepared (oxidized) Micellar Samples Measured in He at RT Together with Their Reduced Counterparts and a Reference Pt Foil Measured in H$_2$ at RT[a]

	samples	path	N1	R (Å)
Pt bulk		Pt−Pt	12.1 (0.2)	2.765 (0.004)
S1	as prepared (in He)	Pt−Pt	8.4 (1.2)	2.763 (0.005)
		Pt−O	0.8 (0.4)	1.97 (0.02)
	reduced (in H$_2$)	Pt−Pt	8.6 (0.2)	2.761 (0.005)
S2	as prepared (in He)	Pt−Pt	4.2 (1.5)	2.76 (0.01)
		Pt−O	1.4 (0.5)	2.02 (0.02)
	reduced (in H$_2$)	Pt−Pt	7.5 (0.3)	2.741 (0.006)
S3	as prepared (in He)	Pt−Pt	8.4 (1.4)	2.764 (0.006)
		Pt−O	1.5 (0.5)	2.01 (0.02)
	reduced (in H$_2$)	Pt−Pt	9.0 (0.3)	2.746 (0.005)
S4	as prepared (in He)	Pt−Pt	10.3 (1.2)	2.764 (0.004)
		Pt−O	0.8 (0.3)	1.98 (0.02)
	reduced (in H$_2$)	Pt−Pt	9.7 (0.4)	2.756 (0.006)
S5	as prepared (in He)	Pt−Pt	10.8 (1.0)	2.764 (0.003)
		Pt−O	-	-
	reduced (in H$_2$)	Pt−Pt	10.4 (0.4)	2.767 (0.006)

[a] Interatomic distances (*R*) measured for both types of samples are also shown.

The EXAFS data of the as-prepared oxidized samples [inset in Figure 5b] were also fit (only Pt−O and 1NN Pt−Pt contributions were considered) and a comparison with the corresponding reduced samples is shown in Table 4. The as-prepared samples were measured only at room temperature, while the reduced samples were also measured between −85 and −108 °C. Nevertheless, a comparison of the structure of the oxidized versus the reduced samples requires that both types of samples are analyzed at the same temperature. To minimize uncertainties in the determination of the coordination numbers of the reduced samples at room temperature, we have applied a multiple-data fit procedure where data at different temperatures were analyzed concurrently by constraining the disorder pa-

rameters to be varied according to the correlated Debye model.[62] As a result, the room temperature data were analyzed with higher accuracy than if processed independently. As can be seen in Table 4, the Pt−Pt coordination numbers in the samples containing the smallest NPs (e.g., S2, where this effect can be best seen outside the error bars) were found to increase after sample reduction, indicating that two different Pt species coexisted in these samples before reduction, Pt-oxide and Pt-metal,[21] since no coarsening (that would also have led to higher coordination numbers) was detected for these samples by TEM upon annealing in H$_2$. In fact, the sample temperature during the H$_2$ pretreatment in the EXAFS cell was always equal to or

(62) Sevillano, E.; Meuth, h.; Rehr, J. J. *Phys. Rev. B* **1979**, *20*, 4908.

smaller than the maximum annealing temperature used for the sample preparation (polymer removal in O_2 below 400 °C) that leads to the "as-prepared" samples. Interestingly, the direct comparison of two samples with analogous average diameter (S1 and S2) reveals that sample S2 has a significantly higher percentage of Pt—O bonding with respect to Pt—Pt bonding before reduction as compared to sample S1. A larger difference in the Pt—Pt coordination numbers before and after reduction is also observed for S2 as compared to S1. These trends suggest the presence of interfacial Pt-oxides in this sample, validating its presumably 2D shape. Therefore, the fact that all of our as-deposited samples are strongly oxidized helps us to gain insight into the NP/support interface as well as NP shape.

6. Conclusions

The structure (size and shape) of small (<2 nm) size-selected micellar Pt NPs synthesized by inverse micelle encapsulation has been resolved by a combination of microscopic (TEM, AFM, STM), and spectroscopic (XANES and EXAFS) tools, all integrated within a self-consistent geometric modeling method.

Our work demonstrates that the NP preparation method plays a key role in the final shape of the synthesized NPs. Following our synthetic approach, NP/support interactions that commonly lead to the stabilization of 2D-raft-like cluster shapes in systems such as Pt/γ-Al$_2$O$_3$ can be overcome, resulting in faceted 3D NPs that are ideal candidates for catalysis applications. Furthermore, our EXAFS data evidence the high degree of atomic ordering that can be achieved in very small NPs (~1 nm) using micelle encapsulation synthetic routes as compared to traditional deposition-precipitation methods. This effect might be in part due to the annealing pretreatment that our micellar samples underwent, but also to their interaction with H$_2$ during the EXAFS measurements. H$_2$ is known to induce NP faceting, and due to their enhanced surface area, our 3D NPs should be more prone to reconstructing under H$_2$ as compared to traditional 2D Pt/γAl$_2$O$_3$ clusters.

The present study highlights the importance of integrated analysis methodology involving multiple complementary techniques,[63] and also the uniqueness of EXAFS, combined with cluster shape modeling, for the extraction of information on cluster shapes in size-selected NP samples. Such insight is crucial for the understanding of structure—reactivity relationships in real-world (3D) nanocatalysts in the ~1 nm size range, since such analysis is outside the resolution range of most complementary techniques (such as STM and AFM for 3D clusters) and constitute a serious challenge for state-of-the-art high-resolution TEM microscopes.

Supporting Information Available: XPS data from the C-1s, Cl-2p, Pt-4d and Pt-4f core level regions of Pt NPs supported on γ-Al$_2$O$_3$ and TiO$_2$(110), histograms of the Pt NP height distributions obtained by AFM [on SiO$_2$/Si(100)] and STM [on TiO$_2$(110)] and of the diameter distributions obtained by TEM [on γ-Al$_2$O$_3$], and additional details on the selection of the model shapes. This material is available free of charge via the Internet at http://pubs.acs.org.

JA101997Z

(63) Billinge, S. J. L.; Levin, I. *Science* **2007**, *316*, 561.